INTERFACE

rsif.royalsocietypublishing.org

Research

Cite this article: Li J, Menguy N, Gatel C, Boureau V, Snoeck E, Patriarche G, Leroy E, Pan Y. 2015 Crystal growth of bullet-shaped magnetite in magnetotactic bacteria of the *Nitrospirae* phylum. *J. R. Soc. Interface* **12**: 20141288.
http://dx.doi.org/10.1098/rsif.2014.1288

Received: 20 November 2014
Accepted: 10 December 2014

Subject Areas:
biomaterials, environmental science, nanotechnology

Keywords:
magnetotactic bacteria, Nitrospirae phylum, bullet-shaped magnetite, crystal growth, biomineralization, micromagnetic property

Authors for correspondence:
Jinhua Li
e-mail: lijinhua@mail.iggcas.ac.cn
Nicolas Menguy
e-mail: nicolas.menguy@upmc.fr
Yongxin Pan
e-mail: yxpan@mail.iggcas.ac.cn

Electronic supplementary material is available at http://dx.doi.org/10.1098/rsif.2014.1288 or via http://rsif.royalsocietypublishing.org.

THE ROYAL SOCIETY PUBLISHING

Crystal growth of bullet-shaped magnetite in magnetotactic bacteria of the *Nitrospirae* phylum

Jinhua Li[1,2,3], Nicolas Menguy[2], Christophe Gatel[4], Victor Boureau[4], Etienne Snoeck[4], Gilles Patriarche[5], Eric Leroy[6] and Yongxin Pan[1,3]

[1]Paleomagnetism and Geochronology Lab, Key Laboratory of Earth and Planetary Physics, Institute of Geology and Geophysics, Chinese Academy of Sciences, Beijing 100029, People's Republic of China
[2]Institut de Minéralogie, de Physique des Matériaux, et de Cosmochimie (IMPMC), Sorbonne Universités—UPMC Univ Paris 06, UMR CNRS 7590, Muséum National d'Histoire Naturelle (MNHN), IRD UMR 206, 4 Place Jussieu, Paris 75005, France
[3]France-China Biomineralization and Nano-structures Laboratory, Chinese Academy of Sciences, Beijing 100029, People's Republic of China
[4]CEMES/CNRS; BP 94347, Toulouse Cedex 31055, France
[5]LPN-UPR20/CNRS, Route de Nozay, Marcoussis 91460, France
[6]France Chimie Métallurgique des Terres Rares, ICMPE, UMR 7182, CNRS, 2-8 rue Henri Dunant, Thiais Cedex 94320, France

Magnetotactic bacteria (MTB) are known to produce single-domain magnetite or greigite crystals within intracellular membrane organelles and to navigate along the Earth's magnetic field lines. MTB have been suggested as being one of the most ancient biomineralizing metabolisms on the Earth and they represent a fundamental model of intracellular biomineralization. Moreover, the determination of their specific crystallographic signature (e.g. structure and morphology) is essential for palaeoenvironmental and ancient-life studies. Yet, the mechanisms of MTB biomineralization remain poorly understood, although this process has been extensively studied in several cultured MTB strains in the *Proteobacteria* phylum. Here, we show a comprehensive transmission electron microscopy (TEM) study of magnetic and structural properties down to atomic scales on bullet-shaped magnetites produced by the uncultured strain MYR-1 belonging to the *Nitrospirae* phylum, a deeply branching phylogenetic MTB group. We observed a multiple-step crystal growth of MYR-1 magnetite: initial isotropic growth forming cubo-octahedral particles (less than approx. 40 nm), subsequent anisotropic growth and a systematic final elongation along [001] direction. During the crystal growth, one major {111} face is well developed and preserved at the larger basal end of the crystal. The basal {111} face appears to be terminated by a tetrahedral–octahedral-mixed iron surface, suggesting dimensional advantages for binding protein(s), which may template the crystallization of magnetite. This study offers new insights for understanding magnetite biomineralization within the *Nitrospirae* phylum.

1. Introduction

Magnetotactic bacteria (MTB) are a phylogenetically and ecologically diverse group of prokaryotes which are well known to perform biologically controlled mineralization (BCM) and magnetotaxis, i.e. navigating along the Earth's magnetic field lines in aquatic environments. They can form nanometre-sized single-domain magnetic crystals (either magnetite (Fe_3O_4) or greigite (Fe_3S_4) or both) within intracellular membrane organelles called magnetosomes and arrange these nanocrystals into chains [1,2]. Magnetosomes are a typical system of organic-mineral interactions in which the magnetosome membrane and membrane-associated proteins direct the nucleation and growth of intramembrane magnetic nanocrystals, resulting in their sizes, morphologies and arrangements being specific to each bacterial species or strain [3,4]. Therefore, the study of crystal nucleation and growth of magnetite or greigite within magnetosome membrane is of great importance for exploring the

molecular mechanism of MTB BCM and magnetotaxis [3–6]. For instance, the correlations between magnetosome mineral habits and the phylogenetic affiliations of MTB have important implications for the evolution of magnetosome synthesis, and thus magnetotaxis [3]. Together with comparative genomic analysis, such study can provide useful clues for the potential function of some genes or proteins in controlling mineral phases and crystal habits of magnetosomes [6]. Such study is also essential for understanding the distinctly mineralogical and magnetic properties of magnetosomes that are of fundamental interests in the detection of fossil remains of MTB (i.e. magnetofossils) in the geological records for palaeomagnetic, palaeoenvironmental and ancient-life studies [7,8]. Additionally, as MTB-producing magnetites are promising novel nanomagnetic materials for biomedical application, the understanding of their formation mechanisms is a major issue for further biomimetic synthesis [9].

Most known cultured and uncultured MTB belong to the *Alpha*, *Gamma*- and *Deltaproteobacteria* classes of the *Proteobacteria* phylum, several uncultured species are affiliated with the *Nitrospirae* phylum and one (strain SKK-01) was recently assigned to the candidate division OP3, part of the Planctomycetes–Verrucomicrobia–Chlamydiae bacterial superphylum [5]. It has been found that there may be a correlation between the composition and the morphology of the magnetosome crystals produced by MTB and their phylogenetic affiliation [3,10]. Magnetotactic *Alpha*- and *Gammaproteobacteria*, the later-diverging classes of the *Proteobacteria*, generally produce cubo-octahedral or elongated prismatic magnetites for instance. Both types of magnetosome crystals exhibit homothetical growth, i.e. a constant width/length ratio of crystals for a given MTB species or strain [11]. By contrast, the more deeply branching phylogenetic groups such as MTB in the phylum *Nitrospirae* and the candidate division OP3, as well as the *Deltaproteobacteria*, are known to synthesize anisotropic bullet-shaped magnetite crystals [12–18]. The bullet-shaped magnetosomes have attracted particular research interest in the past decades because they are generally produced in large numbers in each cell and potentially contribute significantly to sedimentary magnetization [16,19]. Furthermore, the unique morphological and crystallographic features of these crystals have never been observed in abiotic processes, leading support to the idea that bullet-shaped magnetites are the most reliable magnetofossils [14,16,20].

Compared with what has been done for cubo-octahedral and prismatic magnetosomes, the biomineralization process of bullet-shaped magnetosomes has been considerably less studied and still remains an enigma because culturing these bacteria has been unsuccessful until now, with the sole exception of *Deltaproteobacterial* strain RS-1 [18]. In an early seminal study of uncultured bacteria, Mann *et al.* [20] have proposed a two-stage crystal growth for bullet-shaped magnetosome magnetite. This two-step growing mode has also been subsequently confirmed by Isambert *et al.* [11], Li *et al.* [16] and Lefèvre *et al.* [14]. Most of bullet-shaped magnetosomes are found to be elongated along ⟨001⟩ [13,16–18] even though other elongation directions have also been reported including ⟨111⟩ [3], ⟨112⟩ [20], ⟨114⟩ [21] and ⟨110⟩ [11,14]. Commonly, a single or multiple flat {111} face exists at the larger (basal) end of the crystals [14,16–18,20–22]. Despite various observation efforts, the elongation direction and the overall morphology of bullet-shaped magnetosomes may be not unambiguously determined owing to the lack of three-dimensional information inherent in conventional transmission electron microscopy (TEM) observations. Therefore, no growing model has been proposed up to now explaining the generally kinked feature of bullet-shaped magnetosome magnetite, in particular for MTB affiliated within the *Nitrospirae* phylum [15,16].

One of the most intriguing systems for studying the bullet-shaped magnetosome within the *Nitrospirae* phylum is the *Candidatus Magnetobacterium bavaricum* (Mbav), first discovered in sediments from the Lake Chiemsee and Lake Ammersee in southern Germany [15,19,23] and its counterparts MYR-1 recently discovered from the Lake Miyun, China [16,24]. Compared with other MTB, Mbav and MYR-1 are unique due to their large sizes (6–10 µm in length) and the large number (up to 1000) of bullet-shaped magnetosomes per cell which may confer to these MTB the highest magnetic moment/volume ratio of any known microorganism [25]. These magnetosomes are generally kinked and highly elongated and arranged into three to five bundles of chains [15,16]. Using ultramicrotomy and three-dimensional reconstructions by serial focused ion beam (FIB) sectioning, Jogler *et al.* [15] have recently revealed the presence of magnetosome membranes and cytoskeletal magnetosome filaments in Mbav, suggesting a similar membrane-templated synthesis of magnetosomes within the *Nitrospira*-affiliated bacteria as in the *Proteobacteria*. However, the detailed process of crystal growth of magnetosome within Mbav or MYR-1 still remains unknown.

Using advanced TEM techniques from the micrometre down to the atomic scale, we have studied some phenotypical variations of MYR-1 and analysed the micromagnetic properties and the growth sequence of bullet-shaped magnetosomes within MYR-1. From these observations, we propose idealized three-dimensional morphologies including the presence of at least one major {111} face associated with a systematic elongation along the ⟨001⟩ crystallographic direction. Finally, a model concerning the BCM of bullet-shaped magnetite in MYR-1 is discussed in light of recent results of phylogenetic studies.

2. Experimental methods

2.1. Sediment sampling, set-up of microcosms, magnetic collection and sample preparation

Sediment samples from Lake Miyun near Beijing (China) were collected at a water depth of 3–10 m. Microcosms were set up in the laboratory with aliquots of sediment slurry in approximately 600 ml plastic bottles which were stored in dimmed light at room temperature. Each bottle contained about 300 ml of sediment and 100 ml of supernatant water. The quantity and community of MTB in the microcosms were periodically checked with the Bacteriodrome (Petersen Instruments, Munich, Germany) [26]. The microcosms dominated by giant rod bacteria were selected for magnetically concentrating MYR-1 cells with a homemade magnetic separation apparatus [16].

For high-resolution TEM (HRTEM) analyses, the concentrated MYR-1 suspension was deposited onto carbon-coated copper TEM grids or ultrathin carbon-coated holey TEM grids and incubated for about 1 h, after which the grids were washed three times in distilled, deionized water and dried. In order to isolate magnetosomes, whole-cell grid samples were digested with 1 M NaOH solution *in situ* for about 10 min and then gently washed with distilled water and dried. After such pre-treatment, the MYR-1 cells were partially lysed and some

magnetosomes were isolated from the cells and the bundle of chains.

2.2. Chemical mapping

The chemical composition of MYR-1 cells was investigated with whole-cell samples. Conventional TEM and high-angle annular dark field imaging in scanning transmission electron microscope mode (HAADF-STEM) and X-ray energy-dispersive spectroscopy (XEDS) mapping experiments were performed on a JEOL-2100F microscope installed at IMPMC (Paris, France), operating at 200 kV, equipped with a field emission gun, a JEOL detector with an ultrathin window allowing detection of light elements and a scanning TEM (STEM) device, which allows Z-contrast imaging in HAADF mode.

2.3. Electron tomography

Electron tomography (ET) using bright-field contrast is unsuitable for studying three-dimensional morphological characteristics of MTB and magnetosomes due to Bragg reflections [27]. The HAADF-STEM imaging technique proves ideal for tomographic reconstruction as it generates strong contrast that has a fully monotonic relationship with thickness. In this study, HAADF-STEM tomography was performed at the ICMPE-CNRS (Thiais, France) on a FEI Tecnai F20 microscope at 200 kV. Acquisition was made using the Digital Micrograph (Gatan) STEM tomography module, and three-dimensional reconstruction was performed using DigiECT software (http://www.digisens3d.com/fr/logiciel-tomographie/soft/2-3D_Electron_Tomography_Software.html).

2.4. Electron holography

Off-axis electron holography (EH) was performed at the CEMES-CNRS (Toulouse, France) on a FEI Tecnai F20 microscope working at 200 kV, equipped with a field emission gun and a Cs corrector. EH allows recovering the phase of the electron beam that has been modified after interaction with magnetic and electrostatic fields inside and outside a nanostructure. This phase shift in a direction X perpendicular to the electron beam can be expressed as

$$\phi(X) = C_E \int V(x, z)\mathrm{d}z - \frac{e}{\hbar} \iint B_\perp(x, z)\mathrm{d}x\mathrm{d}z, \qquad (2.1)$$

where z is the incident electron beam direction, C_E is a constant dependent on the accelerating voltage of the microscope, V is the electrostatic potential of the sample and $B_\perp$ is the component of the magnetic induction (both inside the sample and in the surrounding leakage fields) perpendicular to z. Holographic reconstruction was performed with the help of homemade scripts using the Digital Micrograph (Gatan). The phase images were obtained by reconstructing the holograms using the Fourier method, where one of the interference terms (side band) is isolated by applying a low-pass filter whose radius defines the spatial resolution of the phase image. In our case, we use 5 nm resolution corresponding approximately to the resolution of our Lorentz lens.

The magnetic and electrostatic contributions can be separated by acquiring two holograms for which the sample has been switched upside down. The half difference of the corresponding phase images give the magnetic contribution to the phase shift [28]. The isophase contour of the magnetic phase shift gives then a direct representation of the projected induction field lines. However, as the phase shift is integrated over the entire path of the electron, the two-dimensional recorded image contains all the information about the internal structure of the domain wall projected along the z-direction.

2.5. High-resolution TEM and atomic-resolution high-angle annular dark field imaging in scanning transmission electron microscope mode

Isolated magnetosome samples were used for HRTEM and atomic-resolution HAADF-STEM imaging. HRTEM experiments were performed at ESPCI (Paris, France) on a JEOL 2010F microscope at 200 kV, equipped with a Gatan cooled CCD camera (1024 × 1024 pixels). For each particle, observed zone axis and in-plane crystallographic direction were determined from the two-dimensional Fast Fourier transform of the HRTEM image, and then allowed us to deduce the corresponding stereographic projection. For immature magnetosomes, i.e. with shapes deriving from a cubo-octahedron, the same procedure as described in [29] was applied to determine the three-dimensional morphology. Owing to the shape complexity and variability, the main morphological features of mature magnetosomes were deduced from HRTEM images recorded from ⟨110⟩ zone axis of magnetite. Idealized shapes modelled with the KrystalShaper software package (available at http://www.jcrystal.com/) were then compared to direct observations.

Atomic-resolution HAADF-STEM was performed at LPN-CNRS (Marcoussis, France) on a Cs-corrected JEOL 2200FS microscope operating at 200 kV. HAADF-STEM image is advantageous for directly interpretable structural analysis because the contrast is atomic number-dependent (approx. $Z^{1.7}$) [30]. In order to improve the quality of the image, Fourier filtering was used [31].

3. Results

3.1. Phenotypical characteristics of MYR-1

HAADF-STEM imaging and STEM–XEDS elemental mapping revealed a phenotypical heterogeneity among MYR-1 cells. Phenotype I contains only magnetosomes, while phenotypes II and III contain two types of inclusions other than magnetosomes. Phenotype II contains globules which exhibit no significant difference in chemical compositions from the cytoplasm but appear almost transparent in HAADF-STEM imaging mode comparing with the surrounding cytoplasm. These vesicles can therefore be interpreted as polyhydroxybutyrate-like or lipid storage particles. Phenotype III produces numerous sulfur-rich globules (figure 1*a–c* and electronic supplementary material, figure S1). These three phenotypes of MYR-1 have also been observed in Mbav and other *Nitrospira*-affiliated strains [13,15,22,23]. They may represent different growth stages of MYR-1 or may be related to physiological states of individual cells or/and local microenvironments.

ET demonstrated that the bullet-shaped magnetosomes are organized into three to five bundles of chains, which are roughly parallel to each other and distribute along the long axis of the cell (electronic supplementary material, movie S1). Each bundle usually consists of two to three magnetosome chains which are approximately parallel to each other. These observations are consistent with the three-dimensional reconstructions of FIB sections of Mbav cells reported by Jogler *et al*. [15]. However, both observations argue against a twisted

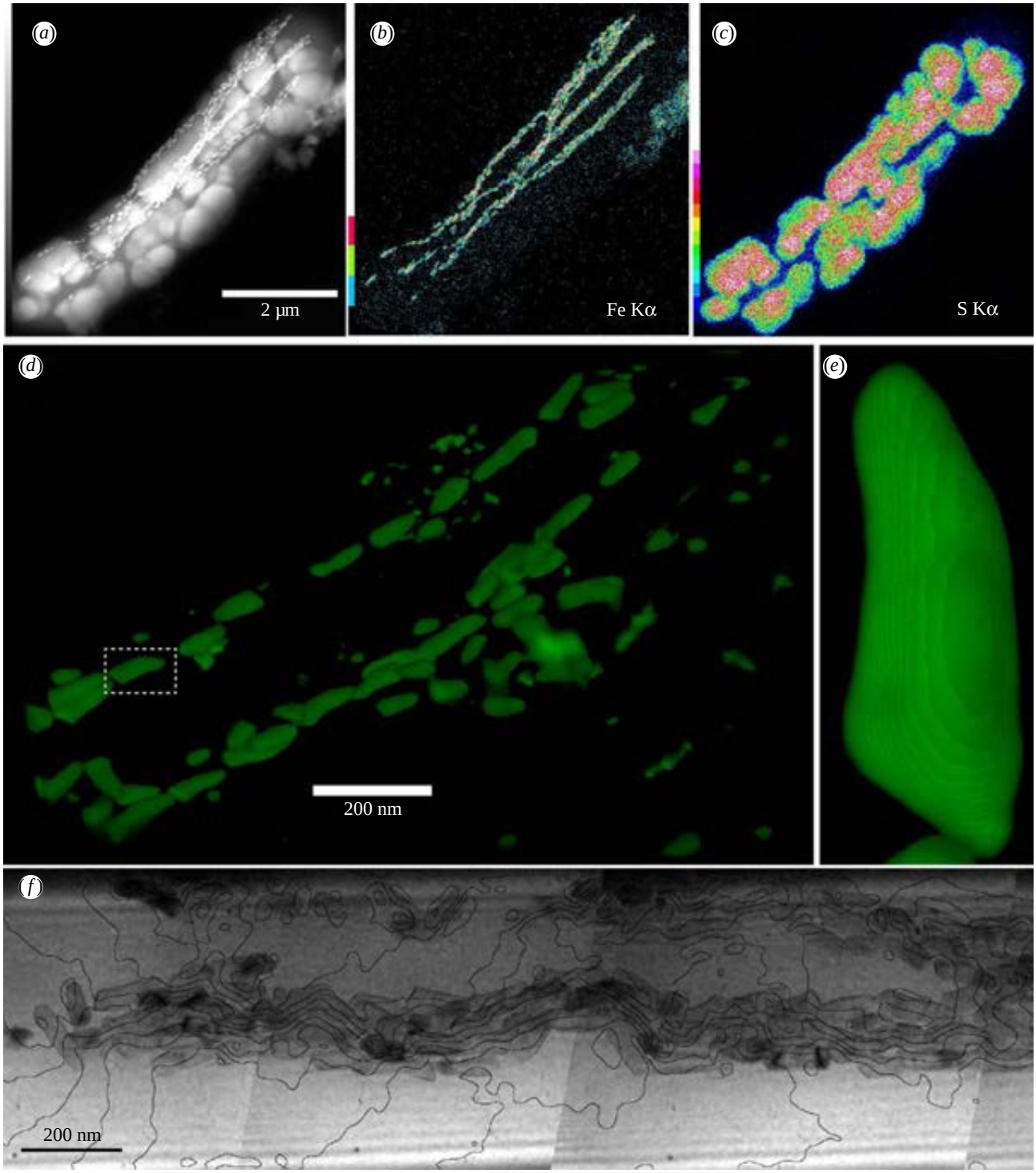

Figure 1. Morphologic, chemical and micromagnetic features of MYR-1. (*a–c*) HADDF-STEM image of MYR-1 cell (*a*) and their corresponding chemical maps of Fe (*b*) and S (*c*). (*d*) HAADF-STEM tomographic image (three-dimensional visualization) of MYR-1 magnetosome chains. (*e*) HAADF-STEM tomographic image of individual particle indicated by the white dashed box in (*d*). (*f*) Magnetic phase contours of MYR-1 magnetosome chains recorded using off-axis EH, formed from the magnetic contribution to the holographic phase, overlaid onto the amplitude phase image of magnetosome chains (to allow the positions of the crystals to be correlated with the magnetic contours). The magnetic phase contour spacing is 1 radian.

'braid-like' helical structure of magnetosome chains, which was described in previous study [21]. Based on a series of HAADF images on a small selected region of magnetosome chains, the three-dimensional shape of crystals can be visualized. Unlike cubo-octahedral and prismatic magnetosomes, which have a relatively well-defined morphology for a given species or strain, MYR-1 magnetite crystals display irregular and various morphologies depending on their sizes (figure 1*d* and electronic supplementary material, movie S2). However, general trends can still be found for mature magnetosomes: (i) at least one flat face is systematically observed at the larger (basal) ends of those elongated particles, (ii) most exhibit a more or less pronounced kinking (figure 1*e*) and (iii), as discussed below, the overall elongation direction is ⟨001⟩.

3.2. Micromagnetic characteristics of magnetosome chains

Off-axis EH was used to study the magnetic microstructure of MYR-1 magnetosome chains. Figure 1*f* shows the contour map

of the magnetic flux within and out of the chains. Although the magnetic induction maps are slightly noisy due to the overall thickness of the MYR-1 (approx. 1.5 µm) and the over stacking of particles making clear visualization of bundle of chains difficult, it can still be seen that the magnetic contours closely correlate with each bundle of chains and the magnetic interactions between two neighbouring bundles are relatively weak (figure 1*f* and electronic supplementary material, figure S2). Within each bundle of chains, the magnetic contours run along the elongation direction of individual particles, i.e. ⟨001⟩, and the overall direction of the magnetic moment is approximately parallel to the chain axis, similar to the EH observations on chains of cubo-octahedral and prismatic magnetosomes [32,33]. Some individual crystals are misaligned relative to their neighbours in the chains (possibly resulting from the collapse of the chains during sample preparation) causing a bending of the magnetic field direction. The EH results show that each bundle of MYR-1 chains appears to behave magnetically as a large uniaxial single-domain (USD) magnet that maximizes the net magnetic moment of the cell to optimize the efficiency of magnetotaxis, consistently with the magnetic measurements on bulk sample of aligned MYR-1 cells [16].

3.3. Crystal growth and atomic structure of MYR-1 magnetite

The process of crystal growth has been investigated by HRTEM observations on 132 magnetosomes covering grain sizes ranging from approximately 10 to approximately 180 nm in length. We assumed that the observed grain size reflects the growth stage of the crystal, i.e. the smallest and the largest ones should correspond to the nascent and mature magnetosomes, respectively. Crystals with size smaller than approximately 10 nm were not found in this study, therefore no information about the very early stage of magnetite biomineralization for MYR-1 has been obtained as it has recently been done for *Magnetospirillum magneticum* strain AMB-1 [34]. From a practical perspective, the thickness of MYR-1 cell and the widespread overlapping of magnetosomes within intact cells make the HRTEM study on individual particles quite difficult. To overcome this obstacle and obtain high-quality lattice images of individual crystals, the MYR-1 cells deposited onto carbon-coated TEM grids were gently lysed *in situ* with 1 M NaOH solution. Using this pre-treatment, the cells were digested on the grid and the magnetosomes were released from the cells and the bundle of chains. TEM observations failed to detect the presence of a TEM-transparent layer enveloping the isolated magnetosomes, suggesting that the digestion procedure had also removed the magnetosome membranes (figures 2*b–g* and 3). A previous study has shown that surface oxidation of magnetite to maghaemite easily takes place during magnetosome isolation at low temperature without protection from oxygen [35]. In this study, both HRTEM and atomic-resolution HAADF-STEM observations reveal that those isolated magnetosomes from MYR-1 cells exhibit crystal and atomic structures consistent with magnetite. No crystal defects such as twinning, stacking-fault and cation vacancies were detected in the isolated magnetosomes observed (figures 2–4). This indicates that no significant oxidization occurs within magnetite crystals during magnetosome isolation. Alternatively, maghaemitization, if it happened, could be subtle and did not change neither the $Fd\bar{3}m$ inverse spinel structure nor the crystal habits.

Figure 2*a* shows a plot of particle length versus width of individual magnetosomes. In agreement with previous observations on bullet-shaped magnetosomes [11,14,16,20], it can be seen that the magnetosome growing within MYR-1 occurs in a two-step process: isotropic growth (up to approx. 40 nm) followed by anisotropic growth, with the latter characterized by unidirectional growth, i.e. particle length increasing with a constant width (approx. 40–45 nm). Figure 2*b–g* shows representative HRTEM images of magnetite crystals smaller than approximately 40 nm, i.e. in the initial isotropic growth domain with a width/length ratio close to 1. Following a method previously used by Faivre *et al*. [29], it can be determined that these nascent crystals are well-crystallized cubo-octahedron with {111} + {100} forms (figure 2*b–d*) or close to truncated cubo-octahedron with {111} + {110} + {100} forms (figure 2*e–g*). It has to be noted that these magnetite morphologies are close to the octahedral equilibrium form and are frequently observed in purely abiotic processes [36].

As their size reach a threshold value of about 35–40 nm, the magnetosomes start anisotropic growth leading to elongated crystals with various morphologies. Figure 3 shows HRTEM images of immature (figure 3*a–d*) and mature elongated crystals (figure 3*e–h*) viewed along $[1\bar{1}0]$ zone axis of magnetite. The identification of the initial elongation direction of magnetosomes is not straightforward due to their complicated morphologies and may be somewhat ambiguous. It can vary from [111], [112], [113], [114], [115] or even [001] among different particles (figure 3; electronic supplementary material, appendix SI). Most importantly, for mature particles, it appears that the final elongation is always along the [001] direction whatever the different initial elongation direction. Furthermore, the offset between the initial elongation direction [*uvw*] and the final direction [001] results in various kink morphologies (figure 3*e–h*). For instance, a small curvature can be observed when the offset is small as shown in figure 3*e*. In this case, the angle between the initial [114] elongation and the final [001] elongation is approx. 19.47° (figure 3*e*). For those particles with [112] or [111] initial elongation, more pronounced kinking or double kinking can sometimes be observed (figure 3*f–h*). The kinking occurs generally at a particle length ranging from approximately 35 to 80 nm, which is usually larger than the onset of anisotropic growth of crystals. For each analysed mature crystals (greater than approx. 80 nm), the width and the length from the centre of the basal end to the kink position were measured following the method by Mann *et al*. [20]. The mean value of the kink distance : width ratio is equal to 1.17 ± 0.27 ($N = 38$). This suggests that the kinking is closely related to the anisotropic growth of magnetosomes as reported by Mann *et al*. [20].

Despite their quite irregular shapes, almost all mature particles preserve at least one flat {111} face at their basal end. Some particles have double-triangle shapes and elongate apparently along the [001] direction. Taking advantage of the informative HAADF-STEM images (electronic supplementary material, appendix SI), it has been possible to obtain some detailed information concerning the morphology of the magnetosomes close to the prominent {111} face. The idealized shapes shown in figure 3*i–l* are examples of what can be observed within MYR-1 magnetosomes. For an initial elongation along [112], two kinds of shapes have been observed. In the first case, the magnetosome morphology is close to a bevelled solid cylinder with a horizontal axis parallel to [112] and with a large $(\bar{1}\bar{1}\bar{1})$ face and a small $(00\bar{1})$ face at the basal end

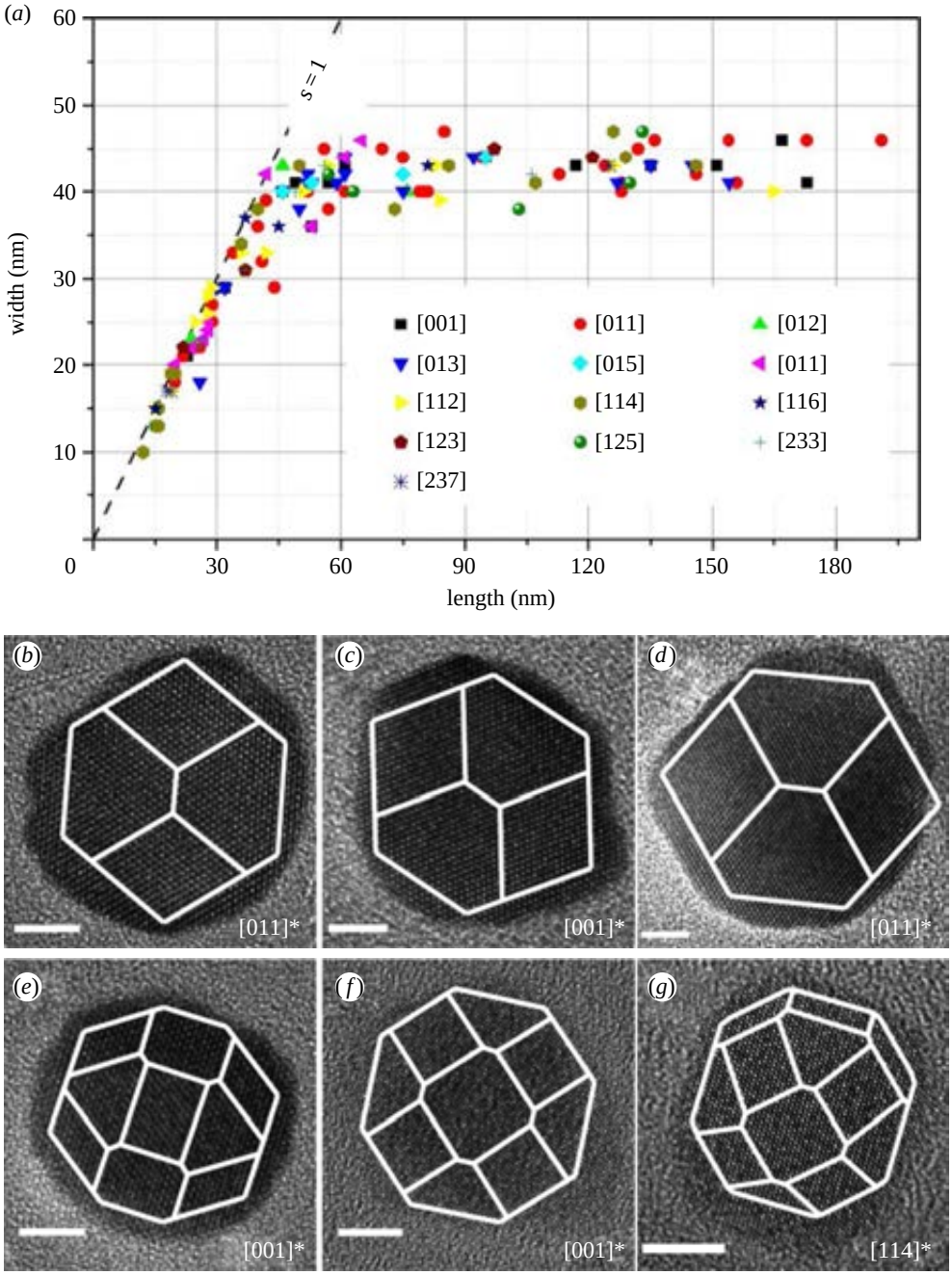

Figure 2. Multiple-step crystal growth of MYR-1 magnetite. (*a*) Plot of crystal length versus width of MYR-1 magnetosomes. The data were measured from HRTEM images recorded for a given zone axis. Different symbols with different colours indicate different zone axes. In total, 132 particles were analysed in this study. (*b–g*) Representative HRTEM images of MYR-1 magnetosomes with crystal size lower than approximately 40 nm and corresponding idealized morphological models. (*b–d*) Particles can be recognized as isotropic crystals composed of {111} + {100} forms (cubo-octahedron), and (*e–g*) of {111} + {110} + {100} forms. Scale bar, 5 nm.

(figure 3*i*,*k*). The second morphology generally exhibits two additional small {111} faces besides one large $(\bar{1}\bar{1}\bar{1})$ face and one small $(00\bar{1})$ face; therefore, this part of the magnetosome appears to be the remains of a cubo-octahedron (figure 3*j*,*l*). As deduced from HAADF-STEM observations, the cross section of magnetite crystals is circular and consequently no defined {*hkl*} Miller indices may be assigned to the lateral faces, i.e. parallel to the elongation direction. These results can be extended to magnetosomes with other initial elongation directions (electronic supplementary material, appendix SI). The upper narrow ends of the crystals appear to be more pointed, while a small (001) face with sharp edge and flat end can still be recognized in some particles (mostly mature ones) by HRTEM and atomic-resolution HAADF-STEM observations (figure 3; electronic supplementary material, appendix SII).

The atomic structure of MYR-1 magnetites was further investigated with HAADF imaging using Cs-corrected STEM (figure 4). Figure 4*b* shows an original atomic-resolution HAADF-STEM image of the basal end of one typical magnetite crystal obtained along $[1\bar{1}0]$ zone axis (figure 4*a*). According to the *Z*-contrast [30], each bright spot in figure 4*b* corresponds to one individual column of iron atoms, while columns of oxygen atoms are not visible. It can be seen that the basal {111} face is flat and well developed at the atomic scale. At higher magnification, the comparison between atomic-resolved images and the crystal structure model shows that the {111} face is made of Fe ions from the mixed octahedral and tetrahedral sites (figure 4*c*). Additional HRTEM and atomic-resolution HAADF-STEM images, illustrating the preservation of a well-developed {111} face at the basal end and the presence of a

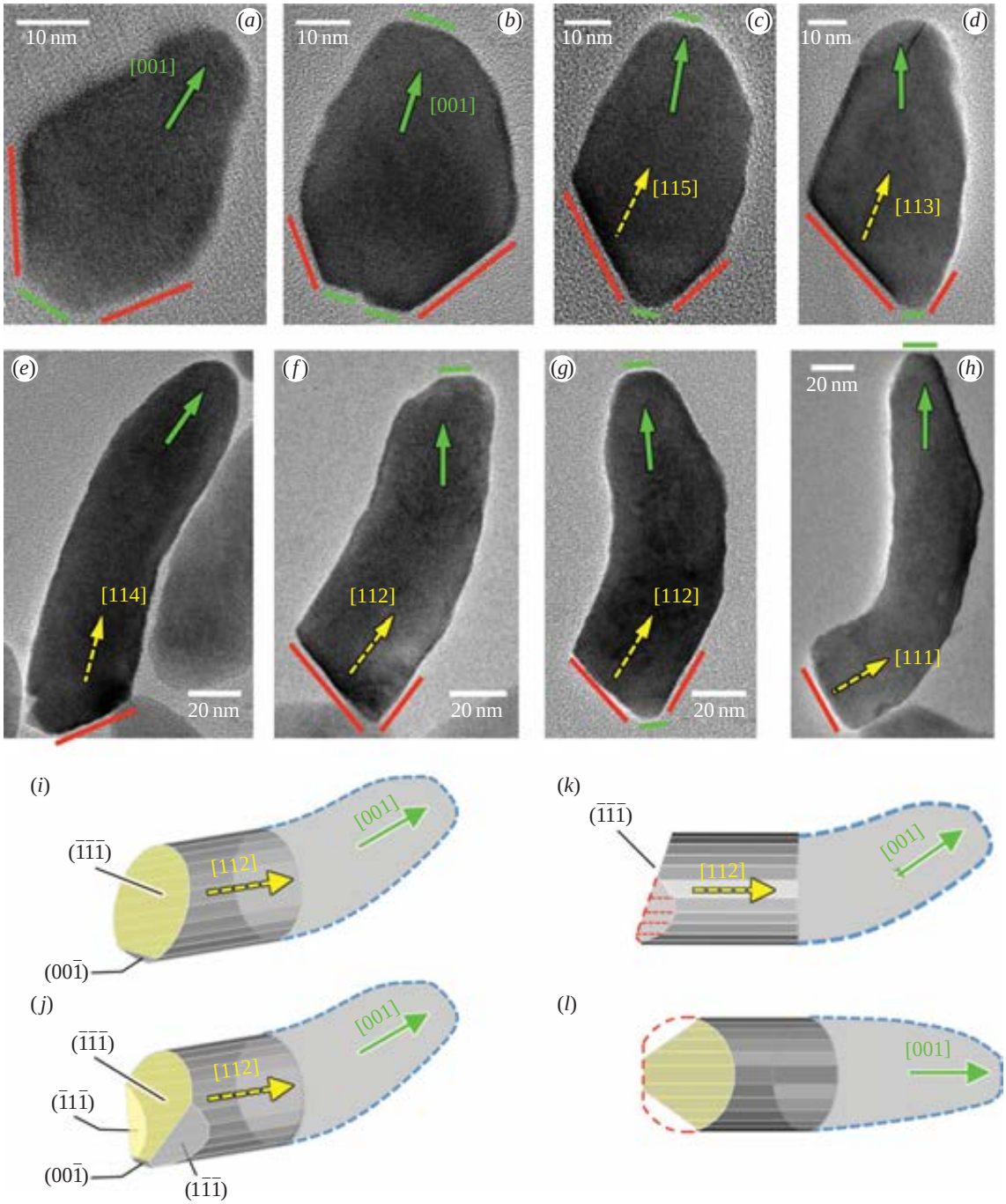

Figure 3. Anisotropic crystal growth of MYR-1 magnetite. (*a–d*) Typical TEM images of immature elongated particles. (*e–h*) Typical TEM images of mature elongated particles. All images were recorded from [1$\bar{1}$0] zone projection of magnetite. (*i–l*) Morphological models for MYR-1 magnetite crystals. (*i*,*k*) Models indicate a bevelled solid cylinder viewed along different orientations. This cylinder exhibits a horizontal axis parallel to [112] and with a large ($\bar{1}\,\bar{1}\,\bar{1}$) face and a small (00$\bar{1}$) face at the basal end. (*j*,*l*) Models are similar cylinder with two additional small {111} faces at the basal end of the particle viewed along different orientations. The red and green lines indicate the {111} and {001} faces, respectively. The yellow dashed arrow line and green arrow line indicate the initial and final elongation directions, respectively.

small {100} face at the top end of mature particles are available in electronic supplementary material, appendix SII.

4. Discussion

4.1. Crystal growth and molecular mechanisms

The magnetosome membrane provides an efficient 'nano-bioreactor' for intramembrane magnetite mineralization, where membrane-associated phosphatidylethanolamines facilitate the nucleation and stabilization of magnetite crystal by interacting with the negatively charged magnetite [37,38]. The magnetosome membrane-associated proteins (MMAPs) play a role in the activation of the magnetosome membrane, magnetosomal iron transport, crystal growth and chain assembly [4]. Recent cryo-ET studies have demonstrated that magnetosome crystal formation appears to be initiated at a nucleation site on the membrane inner surface and that morphologies of magnetosome membranes are consistent with their intramembrane crystals [39], e.g. almost spherical vesicles observed in *Magnetospirillum* species that produce cubo-octahedral magnetite [40,41], and elongated vesicles in *Magnetovibrio blakemorei* that produce elongated prismatic magnetite [39]. Taken together with the information from these previous studies, our study

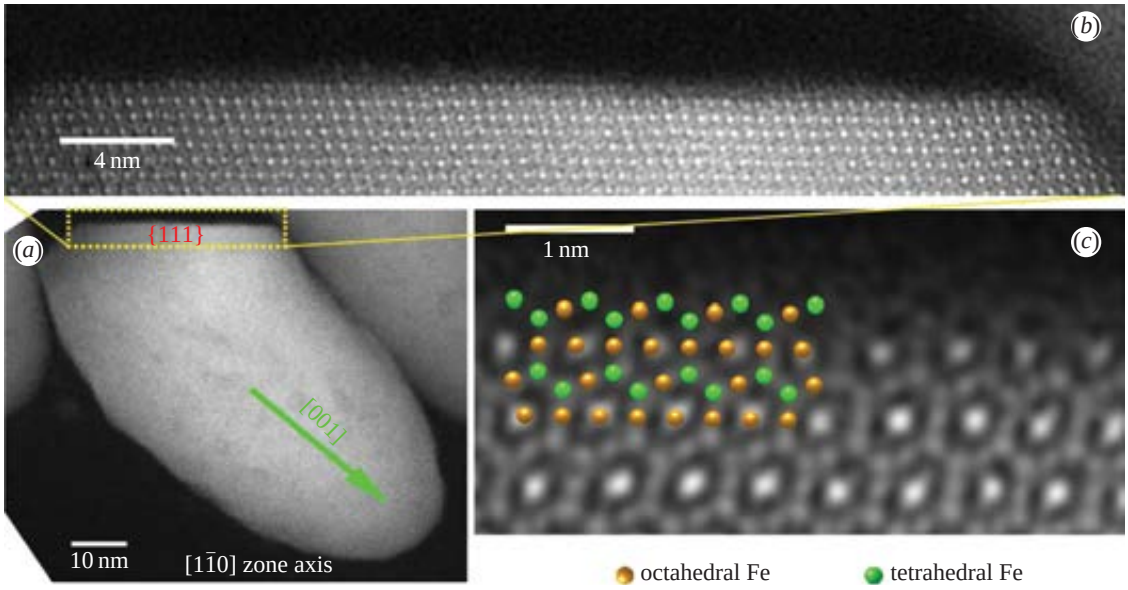

Figure 4. Atomic surface structure of the basal end of MYR-1 magnetite. (*a*) HAADF-STEM image of one particle recorded from [1$\bar{1}$0] zone axis. (*b*) Atomic-resolution HAADF-STEM image of the basal end of this particle indicated by yellow rectangle in (*a*). Each bright spot corresponds directly to one individual column of iron atoms. Columns of oxygen atoms are not visible because the contrast in HAADF-STEM image is atomic number-dependent (approx. $Z^{1.7}$) [30]. (*c*) Comparison of the surface atomic structure of the basal end of MYR-1 magnetite with the theoretical Fe arrangement of magnetite. The image was filtered to remove the noise component in HAADF-STEM image [31]. Direct atomic observations reveal that the basal end {111} face is terminated by a tetrahedral–octahedral-mixed iron surface.

offers new insights for understanding the biomineralization of bullet-shaped magnetosomes within MYR-1.

We propose the following model for the crystal growth of MYR-1 magnetite within magnetosome membranes (electronic supplementary material, figure S3*a*): (i) initial formation of a cubo-octahedral magnetite (less than approx. 40 nm), (ii) subsequent anisotropic growth along various directions of magnetite dependent on individual particles (e.g. [111], [112], [114], [113], [115] or [001]) up to approximately 35–80 nm in length and approximately 40–45 nm in width, and, finally, (iii) kinking and uniform growth along the [001] direction. Specifically, at the initial stage of magnetite biomineralization, the crystal may nucleate from the {111} face at the surface of magnetosome membrane and they grow in a relatively less limited microenvironment due to the fact that the crystals are much smaller than the magnetosome membranes. The crystal growth depends primarily on the surface area that is available for the attachment of ions or ion clusters from the relatively large membrane vesicles, resulting in forming isotropic cubo-octahedral magnetites [36,42]. When the magnetosome crystal grows up to approximately 40–45 nm, the asymmetric magnetosome membrane may limit the isotropic growth of the particle. Our comprehensive TEM observations demonstrate that whatever the initial growth directions, the final elongation direction is always [001]. It is still unknown whether the kinking growth of MYR-1 magnetite originates from the kinked shape of magnetosome membrane or/and multiple-step regulation by specific protein(s) [6,37], or other non-biological influence such as magnetic interactions [21,43,44]. An alternative hypothesis is that the usual cubo-octahedral equilibrium shape of magnetite is related to the fastest growth direction of magnetite, i.e. ⟨100⟩. The systematic elongation along ⟨100⟩ may also be explained by the conjunction of two constraints: the magnetite tendency to grow preferentially faster along ⟨100⟩ directions and the morphology of the magnetosomal membrane.

This study also reveals that the basal end of MYR-1 magnetite is terminated by a well-developed {111} plane. This indicates that the interfacial interaction between the {111} basal face of magnetite and the MMAPs may play an important role in directing subsequent crystal growth and developing a flat end. It is possible that within MYR-1 magnetosome some acidic MMAPs could recognize and bind with the magnetite {111} surface by electrostatic forces between the iron surface atoms and the O-atoms of the carboxyl- and carboxylate-groups of the molecules [45]. Considering the atomic structure of magnetite surface, there are two possible types of iron arrangement for the terminal {111} surface: the type I arrangement has three out of four octahedral sites occupied (Fe_{oct} layer), and the type II arrangement has one-quarter of the octahedral interstices and one-quarter of the tetrahedral sites filled ($Fe_{oct+tet}$ layer) [46]. In this study, direct atomic-resolution HAADF-STEM imaging has shown that the basal {111} face of MYR-1 magnetite starts from a terminal surface of tetrahedral–octahedral-mixed Fe ions, i.e. the type II layer. There are dimensional advantages of such organic–inorganic interface for BCM, as the type II layer may be more suitable for protein binding as a template for crystal nucleation and growth (electronic supplementary material, figure S3*b*). For instance, it has relatively larger Fe–Fe distances than that in Fe_{oct} monolayer, e.g. 3.48 and 3.63 Å for the former and 2.97 Å for the latter, which allows amino acid residues (average diameter approx. 3.4 Å) inserted in this layer as a template for the crystallization of magnetite by adsorbing iron ions or ion clusters [20,47].

The multiple-step crystal growth of magnetite observed in MYR-1 is distinct from that for cubo-octahedral and elongated prismatic magnetosome magnetites in the *Proteobacteria*, which have been demonstrated to have homothetical growth and always elongate along the [111] direction [3,11]. This suggests a different BCM mechanism for MTB from the *Nitrospirae* phylum, at least from the crystallographic point of view.

Very recently, two genomics studies have independently identified a similar genomic cluster containing putative genes responsible for magnetosome formation (i.e. magnetosome island, MAI) within Mbav [15] and MYR-1 (tentatively named as *Candidatus Magnetobacterium*) [48], respectively. The gene profiles in the MAI of MYR-1 are quite different from those in the *Proteobacteria*, although several magnetosome genes including *mamKPMQBAIEQ* show remarkable similarities to their *Proteobacteria* counterparts; six genes (*man1–6*) in the MAI of MYR-1 do not share homology with any known genes and seem to be unique to MYR-1 and/or Mbav [48]. Furthermore, some magnetosome genes such as *mamH-JORSTU*, *mamGFDC*, *mamXY* and *mms6* that are conserved in sequenced *Magnetospirillum* species are missing within the MAI of MYR-1 [48]. It is likely that the unique gene profiles of the MAI in MYR-1 may be involved in the formation of asymmetric magnetosome membrane and multiple-step crystal growth of bullet-shaped magnetite. The paradigm by which the magnetosome membrane provides the nucleation sites, and MMAPs recognize the {111} face, collect iron ions or ion clusters from solution and direct the kinking growth of bullet-shape magnetosome within MYR-1 deserves further investigations. A novel set of culture-independent tools is now available in studying the physico-chemical properties of magnetosome membranes, e.g. atomic force microscopy [49], synchrotron-based scanning transmission X-ray microscopy [47] and cryo-ET [39,50]. Additionally, molecular studies on key MMAPs for magnetite biomineralization are needed in the near future to understand the molecular mechanism of the multiple-step crystal growth for bullet-shaped magnetosomes.

4.2. Magnetic properties and implications for magnetotaxis

For cubic magnetite, the magnetically easy, intermediate and hard directions are the ⟨111⟩, ⟨110⟩ and ⟨100⟩ directions, respectively. Therefore, the most efficient arrangement for the magnetocrystalline anisotropy energy is for the [111] direction to be parallel to the elongation direction of the particle, because the particle then has the largest net magnetic moment per volume possible for magnetite [25]. However, most previous studies have revealed that bullet-shaped magnetite within MTB elongate most along other directions rather than ⟨111⟩ [11,13,14,16–18,20,21]. Consistently with our previous observation [16], this study demonstrates that despite the varieties in the initial direction of crystal growth the final crystal growth of bullet-shaped magnetite within MYR-1 is always along the [001] direction. This non-[111] crystallographic alignment therefore yields net magnetic moments a few per cent lower than the [111] alignment. Yet, MYR-1 produces magnetosomes that in the mature stage are highly elongated with aspect ratio (length/width) close to approx. 4–5 and organized into bundles of chains. The shape anisotropy for an aspect ratio of 1.25 or greater is sufficient to turn the ⟨100⟩ axis of elongation into an effective easy axis and therefore overrides the intrinsic ⟨111⟩ easy axis [43,44]. Therefore, the joint effects of pronounced shape anisotropy and intra-chain magnetic interactions constrain the magnetization direction of individual particles uniformly along the chain axis, evidenced by the EH results. Such crystallographic and magnetic structures of bullet-shaped magnetosomes could help explain why MYR-1 produces a huge number of magnetosomes with highly elongated shapes to increase the total magnetic moment of the cell for efficient navigation along the Earth's magnetic field within sediments [51]; besides magnetosomes might serve also other purposes such as intracellular storage batteries, as postulated by Kopp & Kirschvink [7].

4.3. Phylogenetic and evolutionary issues

Bullet-shaped magnetite is only found in MTB of the more deeply branching phylogenetic groups such as the OP3 candidate division, the *Nitrospirae* phylum and the *Deltaproteobacteria*. This leads to the assumption that bullet-shaped magnetite might have appeared as the first magnetosome [10]. Comparative genomic analysis also shows that a more complicated gene set is probably responsible for bullet-shaped magnetite biomineralization in the *Nitrospira* and *Deltaproteobacteria* than the gene set in the *Alphaproteobacteria* that form cubo-octahedral or prismatic magnetite magnetosome [6,48]. It is likely that during evolution of MTB and/or horizontal gene transfer of magnetosome genes natural selection has provided a pressure to keep or/and develop some genes responsible for forming cubo-octahedral and elongated prismatic magnetosome magnetite with [111] elongation and orientation, which combines the effects of shape anisotropy, magnetocrystalline anisotropy and intra-chain interactions together to optimize the efficiency of magnetotaxis by maximizing the magnetic moment per atom of iron [25,52]. To test this assumption, more biological and geological studies are needed in the near future by identifying more distantly related MTB from other bacterial groups and even from the domain Archaea as well as to identify magnetofossils from very ancient geological records [8].

5. Conclusion

This study reveals a multiple-step crystal growth of magnetite that leads to forming highly elongated and kinked magnetosomes within MYR-1. Despite varieties in the elongation direction at the initial stage of anisotropic growth, the final elongation is uniformly along [001] crystal direction of magnetite. The offset between the initial and final elongation directions results in the formation of various kinked shapes of magnetite crystals.

During the anisotropic crystal growth, one major {111} face at the basal end is well developed and preserved, and it appears to be made of dense monolayer of iron from mixed tetrahedral and octahedral sites. The elongating, kinking crystal growth and the well-defined basal {111} end face together indicate a unique BCM mechanism for bullet-shaped magnetite in MTB of the *Nitrospirae*, which is distinctive from that for cubo-octahedral and prismatic magnetites in the *Proteobacteria*, at least from crystallographic point of view. To determine the molecular mechanisms of the bullet-shaped magnetosome formation and evolution of the magnetosome biomineralization for magnetotaxis, more biological and geological studies are needed on modern MTB and ancient magnetofossils, respectively.

Acknowledgements. We thank Dr Adrienne Kish for her constructive comments and improving the English. We also thank Mrs Xiangzhen Xu (ESPCI, Paris) for assistance in HRTEM experiments. We are grateful to Wei Lin, Yinzhao Wang, Chanqian Cao and Bi Li for their assistance in fieldwork.

Funding statement. This work was supported by the National Natural Science Foundation of China (NSFC grant nos. 41374004, 41330104 and 41004024) and the CAS/SAFEA International Partnership Program for Creative Research Teams (KZCX2-YW-T10). The TEM

facility at IMPMC was supported by Region Ile—de—France grant SESAME 2000 E 1435, INSU—CNRS, INP—CNRS and University Pierre et Marie Curie—Paris 06. The French national network METSA supported by the CNRS is acknowledged for providing the access to the microscope facilities of CEMES in Toulouse. J.H.L. is grateful for support from the China Postdoctoral Science Foundation (CPSC grant no. 201104144) and the French Embassy in Beijing (Sejour Scientifique de Haut Niveau).

References

1. Bazylinski DA, Frankel RB. 2004 Magnetosome formation in prokaryotes. *Nat. Rev. Microbiol.* **2**, 217–230. (doi:10.1038/nrmicro842)
2. Faivre D, Schüler D. 2008 Magnetotactic bacteria and magnetosomes. *Chem. Rev.* **108**, 4875–4898. (doi:10.1021/cr078258w)
3. Pósfai M, Lefèvre C, Trubitsyn D, Bazylinski DA, Frankel RB. 2013 Phylogenetic significance of composition and crystal morphology of magnetosome minerals. *Front. Microbiol.* **4**, 344. (doi:10.3389/fmicb.2013.00344)
4. Komeili A. 2012 Molecular mechanisms of compartmentalization and biomineralization in magnetotactic bacteria. *FEMS Microbiol. Rev.* **36**, 232–255. (doi:10.1111/J.1574-6976.2011.00315.X)
5. Lefèvre CT, Bazylinski DA. 2013 Ecology, diversity, and evolution of magnetotactic bacteria. *Microbiol. Mol. Biol. R.* **77**, 497–526. (doi:10.1128/Mmbr.00021-13)
6. Lefèvre CT *et al*. 2013 Comparative genomic analysis of magnetotactic bacteria from the *Deltaproteobacteria* provides new insights into magnetite and greigite magnetosome genes required for magnetotaxis. *Environ. Microbiol.* **15**, 2712–2735. (doi:10.1111/1462-2920.12128)
7. Kopp RE, Kirschvink JL. 2008 The identification and biogeochemical interpretation of fossil magnetotactic bacteria. *Earth-Sci. Rev.* **86**, 42–61. (doi:10.1016/j.earscirev.2007.08.001)
8. Li JH, Benzerara K, Bernard S, Beyssac O. 2013 The link between biomineralization and fossilization of bacteria: insights from field and experimental studies. *Chem. Geol.* **359**, 49–69. (doi:10.1016/j.chemgeo.2013.09.013)
9. Prozorov T, Bazylinski DA, Mallapragada SK, Prozorov R. 2013 Novel magnetic nanomaterials inspired by magnetotactic bacteria: topical review. *Mater. Sci. Eng. R. Rep.* **74**, 133–172. (doi:10.1016/j.mser.2013.04.002)
10. Lefèvre CT *et al*. 2013 Monophyletic origin of magnetotaxis and the first magnetosomes. *Environ. Microbiol.* **15**, 2267–2274. (doi:10.1111/1462-2920.12097)
11. Isambert A, Menguy N, Larquet E, Guyot F, Valet JP. 2007 Transmission electron microscopy study of magnetites in a freshwater population of magnetotactic bacteria. *Am. Mineral.* **92**, 621–630. (doi:10.2138/am.2007.2278)
12. Kolinko S, Wanner G, Katzmann E, Kiemer F, Fuchs BM, Schuler D. 2013 Clone libraries and single cell genome amplification reveal extended diversity of uncultivated magnetotactic bacteria from marine and freshwater environments. *Environ. Microbiol.* **15**, 1290–1301. (doi:10.1111/1462-2920.12004)
13. Lin W, Li JH, Pan YX. 2012 Newly isolated but uncultivated magnetotactic bacterium of the Phylum *Nitrospirae* from Beijing, China. *Appl. Environ. Microbiol.* **78**, 668–675. (doi:10.1128/AEM.06764-11)
14. Lefèvre CT, Pósfai M, Abreu F, Lins U, Frankel RB, Bazylinski DA. 2011 Morphological features of elongated-anisotropic magnetosome crystals in magnetotactic bacteria of the *Nitrospirae* phylum and the *Deltaproteobacteria* class. *Earth Planet. Sci. Lett.* **312**, 194–200. (doi:10.1016/j.epsl.2011.10.003)
15. Jogler C, Wanner G, Kolinko S, Niebler M, Amann R, Petersen N, Kube M, Reinhardt R, Schüler D. 2011 Conservation of proteobacterial magnetosome genes and structures in an uncultivated member of the deep-branching *Nitrospira* phylum. *Proc. Natl Acad. Sci. USA* **108**, 1134–1139. (doi:10.1073/pnas.1012694108)
16. Li JH *et al*. 2010 Biomineralization, crystallography and magnetic properties of bullet-shaped magnetite magnetosomes in giant rod magnetotactic bacteria. *Earth Planet. Sci. Lett.* **293**, 368–376. (doi:10.1016/j.epsl.2010.03.007)
17. Lins U, Keim CN, Evans FF, Farina M, Buseck PR. 2007 Magnetite (Fe_3O_4) and greigite (Fe_3S_4) crystals in multicellular magnetotactic prokaryotes. *Geomicrobiol. J.* **24**, 43–50. (doi:10.1080/01490450601134317)
18. Pósfai M, Moskowitz BM, Arató B, Schüler D, Flies C, Bazylinski DA, Frankel RB. 2006 Properties of intracellular magnetite crystals produced by *Desulfovibrio magneticus* strain RS-1. *Earth Planet. Sci. Lett.* **249**, 444–455. (doi:10.1016/j.epsl.2006.06.036)
19. Pan YX, Petersen N, Winklhofer M, Davila AF, Liu QS, Frederichs T, Hanzlik M, Zhu RX. 2005 Rock magnetic properties of uncultured magnetotactic bacteria. *Earth Planet. Sci. Lett.* **237**, 311–325. (doi:10.1016/j.epsl.2005.06.029)
20. Mann S, Sparks NHC, Blakemore RP. 1987 Structure, morphology and crystal growth of anisotropic magnetite crystals in magnetotactic bacteria. *Proc. R. Soc. Lond. B* **231**, 477–487. (doi:10.1098/rspb.1987.0056)
21. Hanzlik M, Winklhofer M, Petersen N. 2002 Pulsed-field-remanence measurements on individual magnetotactic bacteria. *J. Magn. Magn. Mater.* **248**, 258–267. (doi:10.1016/S0304-8853(02)00353-0)
22. Lefèvre CT, Frankel RB, Abreu F, Lins U, Bazylinski DA. 2010 Culture-independent characterization of a novel, uncultivated magnetotactic member of the *Nitrospirae phylum*. *Environ. Microbiol.* **13**, 538–549. (doi:10.1111/j.1462-2920.2010.02361.x)
23. Spring S, Amann R, Ludwig W, Schleifer KH, van Gemerden H, Petersen N. 1993 Dominating role of an unusual magnetotactic bacterium in the microaerobic zone of a freshwater sediment. *Appl. Environ. Microbiol.* **59**, 2397–2403.
24. Lin W, Li JH, Schüler D, Jogler C, Pan YX. 2009 Diversity analysis of magnetotactic bacteria in Lake Miyun, northern China, by restriction fragment length polymorphism. *Syst. Appl. Microbiol.* **32**, 342–350. (doi:10.1016/j.syapm.2008.10.005)
25. Vali H, Kirschvink JL. 1990 Observations of magnetosome organization, surface structure, and iron biomineralization of undescribed magnetic bacteria: evolutionary speculations. In *Iron biominerals* (eds RB Frankel, RP Blakemore), pp. 97–115. New York, NY: Plenum Press.
26. Petersen N, Weiss D, Vali H. 1989 Magnetic bacteria in lake sediments. In *Geomagnetism and palaeomagnetism* (eds F Lowes *et al*.), pp. 231–241. Dordrecht, The Netherlands: Kluwer.
27. Buseck PR, Dunin-Borkowski RE, Devouard B, Frankel RB, McCartney MR, Midgley PA, Pósfai M, Weyland M. 2001 Magnetite morphology and life on Mars. *Proc. Natl Acad. Sci. USA* **98**, 13 490–13 495. (doi:10.1073/pnas.241387898)
28. Midgley PA, Dunin-Borkowski RE. 2009 Electron tomography and holography in materials science. *Nat. Mater.* **8**, 271–280. (doi:10.1038/nmat2406)
29. Faivre D, Menguy N, Pósfai M, Schüler D. 2008 Environmental parameters affect the physical properties of fast-growing magnetosomes. *Am. Mineral.* **93**, 463–469. (doi:10.2138/am.2008.2678)
30. Weyland M, Thomas JM, Dunin-Borkowski RE, Midgley PA. 2001 High spatial resolution tomographic reconstruction from STEM high angle annular dark field (HAADF) images. *Electron Microsc. Anal.*, **168**, 107–110.
31. Krivanek OL, Dellby N, Murfitt MF, Chisholm MF, Pennycook TJ, Suenaga K, Nicolosi V. 2010 Gentle STEM: ADF imaging and EELS at low primary energies. *Ultramicroscopy* **110**, 935–945. (doi:10.1016/j.ultramic.2010.02.007)
32. Simpson ET, Kasama T, Pósfai M, Buseck PR, Harrison RJ, Dunin-Borkowski RE. 2005 Magnetic induction mapping of magnetite chains in magnetotactic bacteria at room temperature and close to the Verwey transition using electron holography. *J. Phys. Conf. Ser.* **17**, 108–121. (doi:10.1088/1742-6596/17/1/017)
33. Dunin-Borkowski RE, McCartney MR, Frankel RB, Bazylinski DA, Pósfai M, Buseck PR. 1998 Magnetic microstructure of magnetotactic bacteria by electron holography. *Science* **282**, 1868–1870. (doi:10.1126/science.282.5395.1868)
34. Baumgartner J, Morin G, Menguy N, Gonzalez TP, Widdrat M, Cosmidis J, Faivre D. 2013 Magnetotactic bacteria form magnetite from a phosphate-rich

ferric hydroxide via nanometric ferric (oxyhydr)oxide intermediates. *Proc. Natl Acad. Sci. USA* **110**, 14 883–14 888. (doi:10.1073/pnas.1307119110)

35. Fischer A, Schmitz M, Aichmayer B, Fratzl P, Faivre D. 2011 Structural purity of magnetite nanoparticles in magnetotactic bacteria. *J. R. Soc. Interface* **8**, 1011–1018. (doi:10.1098/rsif.2010.0576)
36. Faivre D, Menguy N, Guyot F, Lopez O, Zuddas P. 2005 Morphology of nanomagnetite crystals: Implications for formation conditions. *Am. Mineral.* **90**, 1793–1800. (doi:10.2138/am.2005.1853)
37. Grünberg K, Müller EC, Otto A, Reszka R, Linder D, Kube M, Reinhardt R, Schüler D. 2004 Biochemical and proteomic analysis of the magnetosome membrane in *Magnetospirillum gryphiswaldense*. *Appl. Environ. Microbiol.* **70**, 1040–1050. (doi:10.1128/AEM.70.2.1040-1050.2004)
38. Baumgartner J, Carillo MA, Eckes KM, Werner P, Faivre D. 2014 Biomimetic magnetite formation: from biocombinatorial approaches to mineralization effects. *Langmuir* **30**, 2129–2136. (doi:10.1021/La404290c)
39. Abreu F *et al*. 2013 Cryo-electron tomography of the magnetotactic vibrio *Magnetovibrio blakemorei*: insights into the biomineralization of prismatic magnetosomes. *J. Struct. Biol.* **181**, 162–168. (doi:10.1016/j.jsb.2012.12.002)
40. Komeili A, Li Z, Newman DK, Jensen GJ. 2006 Magnetosomes are cell membrane invaginations organized by the actin-like protein MamK. *Science* **311**, 242–245. (doi:10.1126/science.1123231)
41. Scheffel A, Gruska M, Faivre D, Linaroudis A, Plitzko JM, Schüler D. 2006 An acidic protein aligns magnetosomes along a filamentous structure in magnetotactic bacteria. *Nature* **440**, 110–114. (doi:10.1038/nature04382)
42. Devouard B, Pósfai M, Hua X, Bazylinski DA, Frankel RB, Buseck PR. 1998 Magnetite from magnetotactic bacteria: size distributions and twinning. *Am. Mineral.* **83**, 1387–1398.
43. Körnig A, Winklhofer M, Baumgartner J, Gonzalez TP, Fratzl P, Faivre D. 2014 Magnetite crystal orientation in magnetosome chains. *Adv. Funct. Mater.* **24**, 3926–3932. (doi:10.1002/adfm.201303737)
44. Nudelman H, Zarivach R. 2014 Structure prediction of magnetosome-associated proteins. *Front. Microbiol.* **5**, 9. (doi:10.3389/Fmicb.2014.00009)
45. Buerger A, Magdans U, Gies H. 2013 Adsorption of amino acids on the magnetite-(111)-surface: a force field study. *J. Mol. Model.* **19**, 851–857. (doi:10.1007/s00894-012-1606-x)
46. Zhu L, Yao KL, Liu ZL. 2006 First-principles study of the polar (111) surface of Fe_3O_4. *Phys. Rev. B* **74**, 035409. (doi:10.1103/PhysRevB.74.035409)
47. Gilbert PUPA, Abrecht M, Frazer BH. 2005 The organic-mineral interface in biominerals. *Rev. Mineral. Geochem.* **59**, 157–185. (doi:10.2138/rmg.2005.59.7)
48. Lin W, Deng A, Wang Z, Li Y, Wen T, Wu L-F, Wu M, Pan Y. 2014 Genomic insights into the uncultured genus '*Candidatus* Magnetobacterium' in the phylum *Nitrospirae*. *ISME J.* **8**, 2463–2477. (doi:10.1038/ismej.2014.94)
49. Yamamoto D, Taoka A, Uchihashi T, Sasaki H, Watanabe H, Ando T, Fukumori Y. 2010 Visualization and structural analysis of the bacterial magnetic organelle magnetosome using atomic force microscopy. *Proc. Natl Acad. Sci. USA* **107**, 9382–9387. (doi:10.1073/pnas.1001870107)
50. Byrne ME, Ball DA, Guerquin-Kern JL, Rouiller I, Wu TD, Downing KH, Vali H, Komeili A. 2010 *Desulfovibrio magneticus* RS-1 contains an iron- and phosphorus-rich organelle distinct from its bullet-shaped magnetosomes. *Proc. Natl Acad. Sci. USA* **107**, 12 263–12 268. (doi:10.1073/pnas.1001290107)
51. Mao X, Egli R, Petersen N, Hanzlik M, Zhao X. 2014 Magnetotaxis and acquisition of detrital remanent magnetization by magnetotactic bacteria in natural sediment: first experimental results and theory. *Geochem. Geophys. Geosyst.* **15**, 255–283. (doi:10.1002/2013gc005034)
52. Pósfai M, Kasama T, Dunin-Borkowski RE. 2007 Characterization of bacterial magnetic nanostructures using high-resolution transmission electron microscopy and off-axis electron holography. In *Magnetoreception and magnetosomes in bacteria* (ed. D Schüler), pp. 197–225. Berlin, Germany: Springer.